JOURNAL OF COMPUTATIONAL PHYSICS 19, 280–296 (1975)

Improved, Implicit Radiation Hydrodynamics

M. T. SANDFORD II, R. C. ANDERSON, H. G. HORAK, AND J. W. KODIS

University of California, Los Alamos Scientific Laboratory,
Los Alamos, New Mexico 87544

Received November 5, 1974; revised February 24, 1975

Improvements to the two-dimensional radiation hydrodynamics method previously reported by Sandford and Anderson consist of an implicit, near-Lagrangian hydrodynamics scheme and grey, implicit and nongrey, explicit S_n methods for radiation transfer. This paper presents as a test problem the radiative-hydrodynamic evolution of two coaxial hot bubbles in the terrestrial atmosphere. The nongrey Monte Carlo and nongrey S_n methods produce very similar radiative evolution. The calculations show that the lower bubble's material is entrained by the ring vortex flow inside the top bubble, where mixing occurs.

I. INTRODUCTION

The equations governing the radiative and inviscous hydrodynamic flow of a gaseous medium in cylindrical geometry were given in our previous paper [1]. The basic equations that we address in this paper are unchanged; but we employ improved hydrodynamics, further discuss the application of the implicit Monte Carlo method, and present S_n methods that can be used to replace or to extend the Monte Carlo method.

Improvements in the hydrodynamics result from our use of the YAQUI algorithm developed by Hirt, Amsden, and Cook [2]. This method results in less numerical diffusion and better numerical stability than the ICE algorithm [3] that we previously employed. The overall coupling of the hydrodynamics and radiation (REEFER) methods is complicated by the quadrilateral cell geometry that results from the near-Lagrangian form of the YAQUI algorithm. This geometry does not restrict the use of Monte Carlo radiation transport, but prevents application of the S_n method, because the latter is formulated in two dimensions for radially aligned mesh cells with rectangular [4] and triangular [5] cross sections. We therefore apply the former (MC) method for cases where numerical diffusion must be minimized through the use of distorted mesh cells; and we use the continuously rezoned Eulerian form of the YAQUI algorithm, together with the grey implicit or nongrey explicit S_n methods, for cases where better radiative stability is needed.

The manner in which we divide a timestep of the fluid is now more complicated, although a computational cycle still consists of alternation between hydrodynamic and radiative flow. The total time step is

$$\Delta t = \max(\Delta t_h, \Delta t_r), \tag{1}$$

and is obtained by performing either one hydrodynamic timestep, Δt_h, or one radiation timestep, Δt_r, and subcycling the other calculation as necessary to complete the cycle. The hydrodynamic timestep is computed from the YAQUI stability conditions such that the maximum number of pressure iterations will approach 20 (cf. Hirt *et al.* [2, Eqs. (22), (23)]). The radiation timestep is found by evaluating the largest fractional change in mesh cell specific internal energy that occurred during the previous timestep, and adjusting the timestep to keep this change near 15 % for the next cycle. Thus we write for the radiative timestep:

$$[(\delta E/\delta t_{\text{old}})/E] \cdot \delta t_{\text{new}} = 0.15, \tag{2a}$$

or

$$\delta t_{\text{new}} = (0.15E/\delta E)\, \delta t_{\text{old}}, \tag{2b}$$

where E is the internal energy in the cell that was found to have the maximum change, δE. Since the maximum specific internal energy change occurs in regions where the material opacity varies to cause cells to range from optically thick to thin, the timestep we compute via Eq. (2) approximates the timestep prescription that we previously employed (cf. [1, Eq. (23)]). The present formulation has the advantages of being simpler to calculate, and of guaranteeing an acceptable timestep. The timestep prescription based solely upon the material properties cannot always control the statistical energy variations that occur when the Monte Carlo method is employed.

We find that global energy conservation to better than 10 % is difficult to obtain if we employ the temperature advancement equation (cf. [1, Eq. (15)]). The temperatures obtained in this manner are indeed correct; but the time-advanced cell energies require double interpolation from the equation of state, and consequently energy is not well conserved. We now utilize the scheme suggested by Fleck and Cummings [6, Eq. (1.17)], which time-advances the material energy. Temperatures are then found from the time-advanced energy and the density by inverting the equation of state tables. This procedure conserves material energy to about 1 %. The temperature advancement scheme that we previously employed may, however, be superior for problems in which the mesh energy is largely contained in the radiation field; for other applications the energy scheme is preferred.

II. Implicit Radiative Transfer

The implicit formulation of the radiative transfer problem introduces fictitious scattering which can often be handled to advantage by the Monte Carlo method [6]. The interaction between the statistical fluctuations inherent in Monte Carlo results and the hydrodynamic calculations can, however, produce nonphysical results. The S_n transport method eliminates these fluctuations because it is a difference method, and hence produces continuous results if stability conditions are obeyed and sufficient order n is employed. The basic equations to be solved assume pure absorption and local thermodynamic equilibrium (L.T.E.) [1], and are directly solvable with the S_n method. The scattering introduced by an implicit formulation complicates the application of the S_n, but should result in a more advantageous timestep [1, p. 137].

The principal complexity in applying the S_n method in the implicit mode occurs in the nongrey problem which requires scattering in energy. The emission function (source term) in the equation of transfer takes the monochromatic form [1, Eq. (18)]:

$$\epsilon_\nu{}^n(\mathbf{r}, t) = \frac{1}{4\pi}\int_0^\infty d\nu' \oint_0^{4\pi} \Sigma_S(\nu', \nu)\, I_{\nu'}{}^n\, d\boldsymbol{\Omega}' + \sigma_{\nu a} b_\nu u_r{}^n, \tag{3}$$

where $I_{\nu'}^n \equiv I_{\nu'}^n\,(\mathbf{r}, \boldsymbol{\Omega}', t)$ is the specific monochromatic intensity at position $\mathbf{r}$, in direction $\boldsymbol{\Omega}'$, at time t^n, for light with frequency ν'; and $\sigma_{\nu a}$ is the effective monochromatic absorption coefficient, b_ν is the normalized Planck frequency distribution, and $u_r{}^n$ is the radiation energy density at timestep n at $\mathbf{r}$.

The scattering coefficient Σ_S appearing in Eq. (3) is given in terms of the implicitness parameter α, the radiation derivative β, and the Planck mean absorption coefficient σ_p, all of which are defined in Ref. [1]. In the case where the implicitness parameter is chosen as zero, the first term on the right in Eq. (3) vanishes, and $\sigma_{\nu a}$ becomes the real absorption coefficient. Thus, an explicit radiation calculation ($\alpha = 0$) may be performed with the multigroup S_n method applicable to pure absorption problems; this method was used to obtain the nongrey S_n results of this paper. A partial or fully implicit ($0 < \alpha \leqslant 1$) solution requires that the scattering of photons from one frequency group to another be considered; the Monte Carlo method is then especially advantageous because the photon frequency can simply be played as a random variable [1, 6]. The implicit S_n method is equivalent to that normally used for neutron problems with both scattering and absorption.

To investigate the combination of YAQUI hydrodynamics with an implicit S_n method, we have applied the latter in the grey atmosphere approximation. The frequency scattering is of course absent in this case, and the emission function, obtained by integrating Eq. (3) with the aid of the definitions given in [1], becomes

$$\epsilon^n(\mathbf{r}, t) = \int_0^\infty \epsilon_\nu{}^n(\mathbf{r}, t)\, d\nu = \bar{\omega}_0 \int_0^{4\pi} \frac{d\boldsymbol{\Omega}'}{4\pi} \int_0^\infty \sigma_{\nu'} I_{\nu'}^n\, d\nu' + (1 - \bar{\omega}_0) \int_0^\infty \sigma_\nu B_\nu\, d\nu \tag{4}$$

$$= \bar{\omega}_0 \sigma \int_0^{4\pi} I^n \frac{d\boldsymbol{\Omega}'}{4\pi} + (1 - \bar{\omega}_0)\, \sigma B, \tag{5}$$

where σ is the grey absorption coefficient, and the scattering albedo is defined [1] by

$$\bar{\omega}_0 = \alpha\beta c\, \Delta t_r \sigma / (1 + \alpha\beta c\, \Delta t_r \sigma). \tag{6}$$

The S_n method is thus required to iterate a grey source function that involves isotropic, nonconservative scattering—a task for which it is well suited [4]. In the explicit limit ($\alpha = 0$) the scattering albedo is zero [Eq. (5)], and the grey emission function becomes that for pure absorption:

$$\epsilon^n(\mathbf{r}, t) \equiv \sigma B. \tag{7}$$

Many physical problems are not adequately represented by the grey atmosphere approximation. We find by comparison between grey S_n solutions using Planck and Rosseland mean absorption coefficients and the other methods that the differences in the radiated power are often very significant, even though the differences in temperature structure are minor. Such conclusions depend on the behavior of the absorption coefficient with temperature and density, and the degree to which radiation couples with hydrodynamics. We therefore recommend that the investigator compare grey with nongrey solutions before discarding the former approximation.

There is a fundamental difference between the Monte Carlo and S_n methods in the manner of mesh usage. The S_n method assumes that the source function and opacity are both constant throughout each mesh cell, and calculates the intensity field by directly solving the equation of transfer across each cell. Provided the number of streams is sufficient, the net flux for each cell is very well determined. The accuracy of the results, insofar as the physical problem is concerned, depends upon the ability of the mesh to represent the material properties. The Monte Carlo method, on the other hand, allows the source function and opacity to vary across each mesh cell according to a systematic procedure (interpolation) which in essence allows the material properties to connect continuously to those in the adjoining cells. The YAQUI hydrodynamics makes use of average properties over each cell, but when used in the near-Lagrangian mode (deformed cells) coupled to the Monte Carlo, one abtains an advantage in resolution as compared to the same number of cells used in the S_n-Eulerian mode. The initial conditions used in these test problems all have the same grid spacing.

III. NUMERICAL EXAMPLE

The radiative transfer process affects hydrodynamic motion by cooling hot regions, thus reducing the gas pressure gradients, and by heating cold regions, causing an increase in pressure. Hydrodynamic motion affects radiative cooling by changing the material density and, hence, effecting change in the opacity. Astrophysical and some other specialized applications consider problems in which the radiation energy density is so large that radiation pressure drives the hydrodynamic motion. Examples of such situations are the circumstellar dust envelopes of cool, giant stars and the extended atmospheres of close binary stars.

Previously [1] we gave calculations that show the evolution of a 15-m-diameter, 1-eV-temperature bubble in air. In this paper we compare the S_n and nongrey Monte Carlo methods by solving two identical bubbles configured to display the advantages of YAQUI hydrodynamics. The Eulerian method used previously, and still required for application of the S_n method, seriously diffuses signals in large cells. Thus, while Eulerian hydrodynamics efficiently calculates the evolution of a single, isolated bubble, the shock interactions that are introduced by considering a reflection boundary and a second coaxial bubble require more computing cells than are needed by a near-Lagrangian scheme.

In this section we discuss the radiative and hydrodynamic evolution of two 30-m-diameter, 1-eV-temperature bubbles that are initially coaxial on the vertical axis one diameter apart, with the lower bubble one diameter above a hydrodynamic reflection boundary. The equations of state and opacities are those for air; we use an exponential atmosphere, and the Earth's gravitational acceleration is included. The lower reflection boundary (the ground) reflects hydrodynamic signals, and has zero albedo; i.e., it absorbs all incident radiative energy. The hot bubbles therefore provide the only radiation source in the problem. The radiant power is calculated from the outward fluxes that leave the computing mesh. The Monte Carlo calculation evaluates these fluxes by scoring the random variables (energy and photon frequency) of statistical particles that escape the mesh. The S_n method calculates the fluxes by integrating the specific intensity (radiance) which is evaluated throughout the computing mesh.

Solutions of the test problem presented in this section were obtained with the implicit, nongrey Monte Carlo, the implicit, grey S_n, and the explicit, nongrey S_n methods. The hydrodynamics scheme consists of the YAQUI algorithm reported in [2]; and this was used in the near-Lagrangian mode with the Monte Carlo calculations, and in the variable-mesh Eulerian mode with the S_n solutions.

The Monte Carlo radiation solution utilized 10 source particles in each cell with temperature above 0.05 eV, but a splitting algorithm prevents particles from terminating their histories if they retain more than 15 % of the minimum mesh cell internal energy. Source particles used in our numerical example numbered approximately 1800 per timestep. The scattering albedo introduced by the implicit formulation results in about three collisions per particle. The computer code requires 10 msec[1] to complete the random walk for an average particle; and the complete radiation cycle requires about 60 sec of computing time. The photon energy (frequency group) is played as a random variable in these calculations so that the computing time is independent of the number of frequency points that we use to describe the absorption coefficient.

The S_n calculations were performed with a code that is not yet fully optimized in assembly language to the CDC-7600 processor, but it appears that the S_n calculations can be made to proceed about 10 times faster than the equivalent Monte Carlo solution. We find that 12 quadrature angles (S_4) produce uniform flux corrections that do not display the ray effect. The scattering iterations demanded by the implicit formulation usually converge in less than 20 iterations. Neither the Monte Carlo nor the S_n method is useful when employed in a code completely programmed in fortran because the running time for even simple problems such as the one discussed here is about 100 hr. The problem we present required about 30 hr for the nongrey Monte Carlo solution and about 6 hr for the nongrey S_n calculation, with a version that employs assembly language selectively in the areas that are most time consuming.

The bubbles' radiative cooling proceeds rapidly compared to the hydrodynamic evolution. The principal coupling between radiation and fluid flow occurs in the bubble centers which are first cooled by radiation and, later, by adiabatic expansion. Figure 1 shows the initial distributions of specific internal energy, density, and velocity in the computing mesh.

Specification of the physical time appropriate to the initial conditions (Fig. 1) is difficult because the bubbles we use are nonphysical entities. The conditions that we show in Fig. 1 result in 0.28 TJ total energy. Our calculations begin with small (~0.1 msec) timesteps and evolve the bubbles forward in time. The mesh variables are relatively static until the "physical" time for the initial conditions is reached, and they then begin to evolve. Similar initial conditions could result from the explosive detonation of gas-filled balloons.

We find that the radiative cooling is different than that obtained previously [1]. The bubbles in this problem do not show the cooling wave previously found. This phenomenon is strongly dependent on the air absorption data, and new values were used for the calculations presented here. Other calculations with the new data show that the cooling wave occurs in bubbles having higher initial temperatures, and at higher altitudes.

The thermal power vs time curve in Fig. 2 shows that radiation begins to cool

---

[1] All calculations presented here were performed on the CDC-7600 computer using the LASL operating system (CROS).

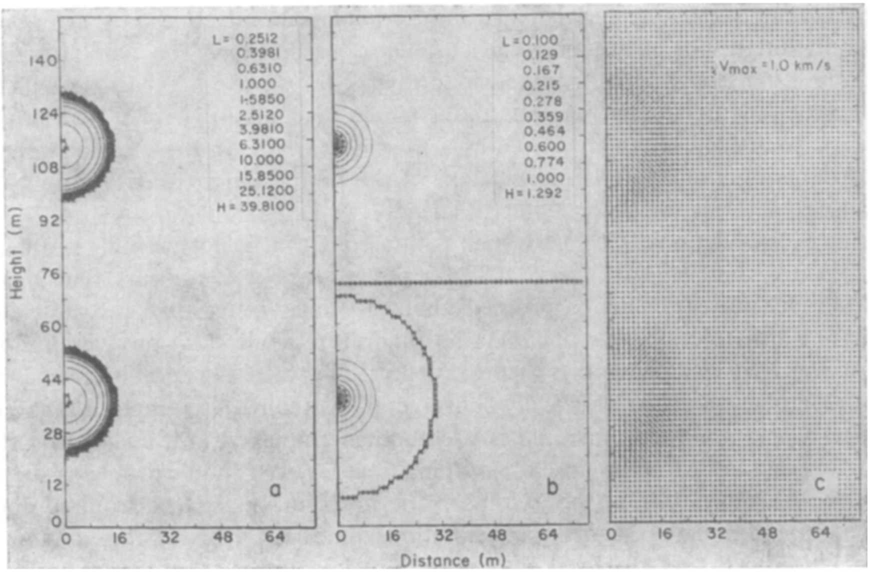

FIG. 1. Initial conditions in the 50 × 100 cell computing mesh for two hot bubbles. (a) Specific internal energy in units of kJ/g at logarithmic contour intervals. (b) Density in units of mg/cm³ at logarithmic contour intervals. (c) Velocity vector plot scaled to the maximum value 1 km/sec.

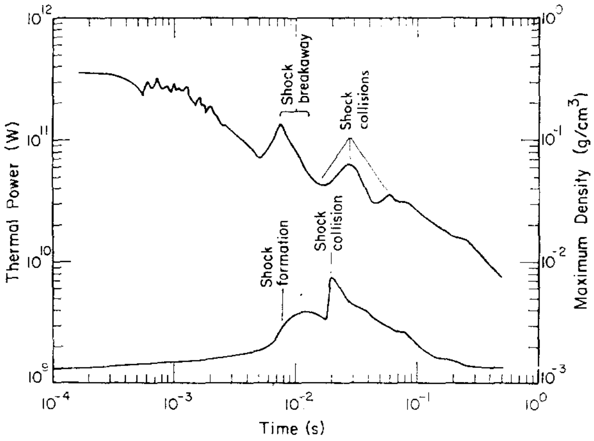

FIG. 2. Thermal power (upper curve) and maximum density (lower curve) vs time.

the bubbles, causing a noticeable decrease in radiated power at about 1.0 msec. The initial linear velocity profile snowplows air until a shock is formed at 12.5 msec; a similar result was obtained in the earlier calculations. This effect is seen in the gradual rise of the maximum density in Fig. 2. Comparison of the initial velocity plot in Fig. 1c with Fig. 5a shows the shock structure. The air absorption coefficient in the bubble edge is especially sensitive to density, and a thermal power peak is seen in Fig. 2 at 7.5 msec when the shock formation begins. This peak is not seen in both S_n calculations which, unlike the Monte Carlo, have opacity "rims" surrounding the bubbles. This opaque "rim" is attributed to the greater numerical diffusion in density that is present in the Eulerian hydrodynamics used with the S_n methods. Figure 3 plots the temperature and density profiles calculated with near-Lagrangian, Monte Carlo methods in the upper bubble at 7.5 and 10.0 msec, and shows the bubble portion that contributes most of the thermal radiation. As the blast wave moves away from the hot bubble, the emission enhancement by density is removed and the pulse in the thermal power vs time curve decays. This is indicated as the "shock breakaway" portion of the thermal power curve (Fig. 2).

Radiative cooling begins at 1.5–2.0 msec, at which time the bubbles are optically very thick, and ends at about 250 msec when the bubbles are optically thin. The

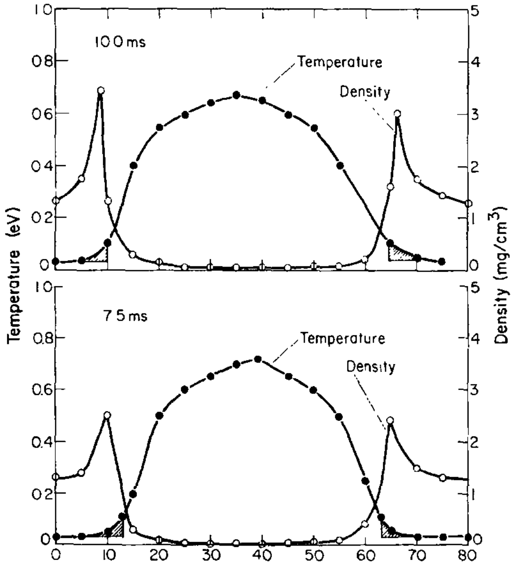

FIG. 3. Vertical profiles of temperature and density in the upper bubble at 7.5 and 10.0 msec. The shaded areas under the temperature curves indicate the regions that are effective in producing radiated power.

power time curve (Fig. 2) shows a change in mean slope at this time. The bubble cores cool uniformly without evidence of a cooling wave. The temperature gradient in the outer, optically thin layers remains constant during the cooling process. Figure 4 shows the cooling curve which plots the maximum (central) temperature vs time. The central Planck mean absorption coefficient is also plotted. The absorption coefficient is an extremely sensitive function of the temperature, and it decreases rapidly as the cooling progresses. We find subsequent opacity oscillations that correspond with those in temperature (the first peak of opacity oscillation is shown in Fig. 4), and density (Fig. 2, lower curve). An optical signature in the thermal power curve results from these slight changes in temperature and density which are caused by shocks colliding. These oscillations in the thermal power occur in both the nongrey Monte Carlo and the grey and nongrey S_n calculations.

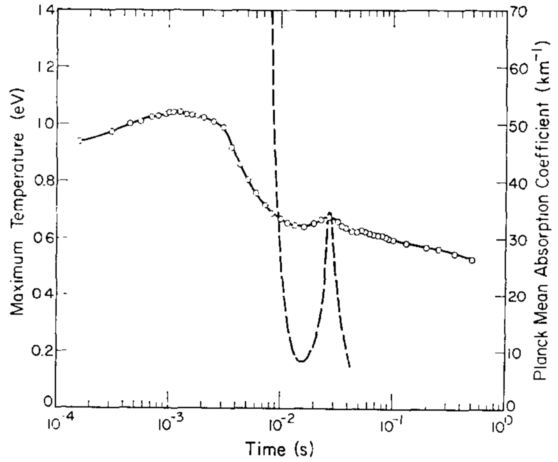

FIG. 4. Bubble cooling curve. The solid curve shows the maximum (central) bubble temperatures vs time. The dashed curve shows the concurrent values of the central absorption coefficient.

At 20 msec the blast waves from the upper and lower bubbles collide, and that of the lower bubble strikes the ground. The thermal-power and maximum density curves (Fig. 2) show definite rises at this time, and both Monte Carlo and nongrey S_n show these, as well as the later oscillations.

We show in Fig. 5 a series of velocity vector plots that cover the interval 10–100 msec; one sees that the hydrodynamic evolution begins with symmetry about a plane perpendicular to the z-axis, equidistant between the bubble centers. The plot at 40 msec shows that the expanding shocks collide between the bubbles and reflect from the symmetry plane. One reflected shock transits the upper bubble

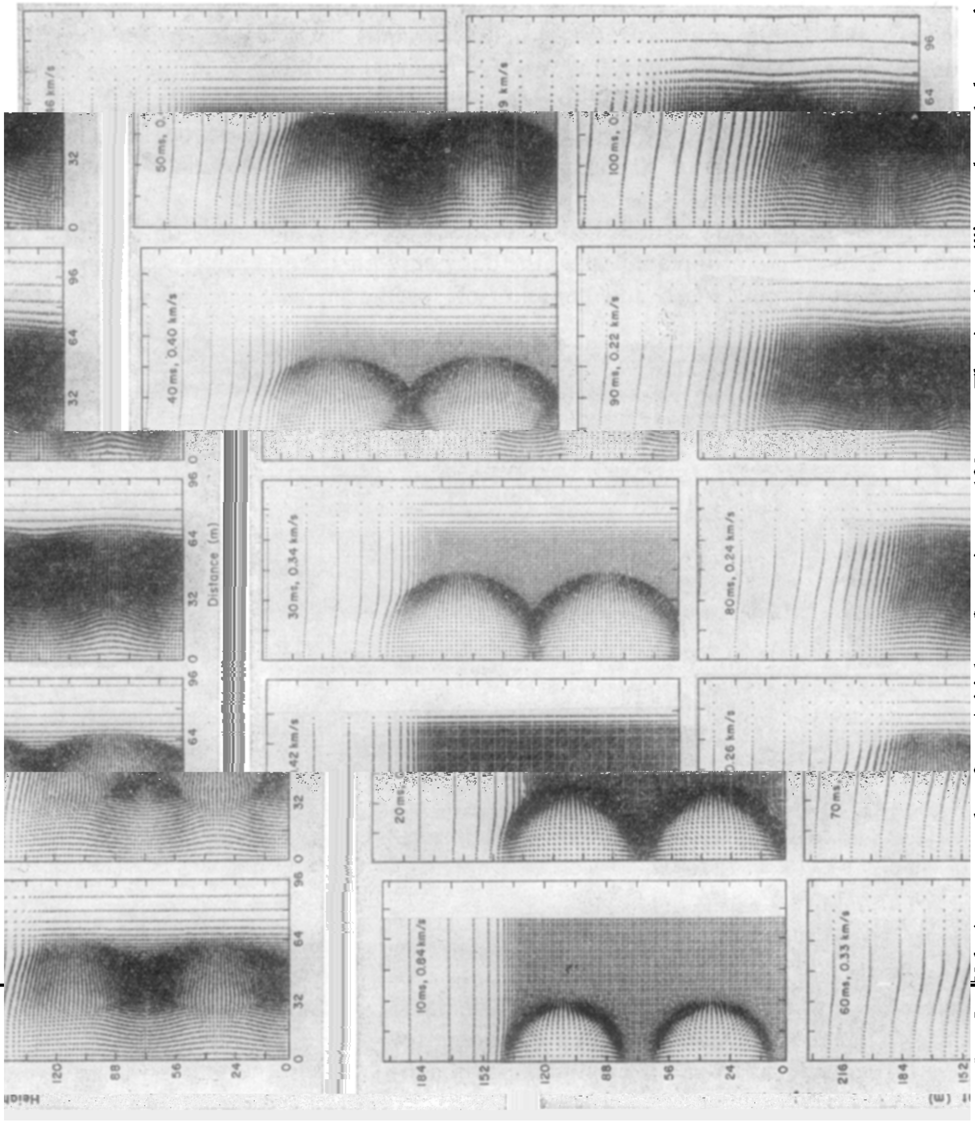

FIG. 5. Velocity vector plots from initial configuration to 100 msec. The time in milliseconds and the maximum flow speed are shown for each plot. The vectors' lengths are scaled to the maximum speed in each plot.

distorting its bottom side, and the other moves downward through the lower bubble distorting its top side. The shock moving downward from the lower bubble reflects from the mesh boundary (the ground) and compresses the lower bubble from below. The colliding shocks produce triple points above and below the symmetry plane, and one also forms near the ground. These points (Mach stem ends [7]) propagate horizontally, and are seen from 60 to 100 msec in Fig. 5. The Mach stems are lost to numerical diffusion as they enter the larger mesh cells.

The reflected ground shock collides with the shock reflected from above at the center of the lower bubble at about 50 msec (refer to Fig. 2). The subsequent evolution is complicated when the shocks compress the lower bubble.

Fluid flow in the upper bubble is established as a clockwise vortex and upward along the z-axis. The shock distortion accelerates the buoyant vortex formation [1]. Figure 6 shows the computing mesh and contours of specific internal energy, density, and vorticity (defined by $| \nabla \times \mathbf{v} |$) at 100 msec. The latter plot illustrates two countercirculation patterns in the lower bubble, and the negative vorticity that is usual in the formation of a toroidal flow field in the upper bubble. One notes the similarities of the negative vortices in the upper and lower bubbles. The isotherms and isopycnics show the severe distortion suffered by the lower bubble as a consequence of the blast wave reflected from above and below.

FIG. 6. (a) The YAQUI computing mesh at 100 msec. (b) Logarithmic contours of specific internal energy in J/kg. (c) Logarithmic contours of density in mg/cm^3. (d) Contours of scalar vorticity. Stippling indicates regions of negative (clockwise) vorticity.

Figure 7 displays surface plots of the specific energy and the total pressure in the computing mesh at 100 msec. The pressure plot illustrates that the individual blast waves coalesce during the 10–100 msec interval to form an expanding, ellipsoidal

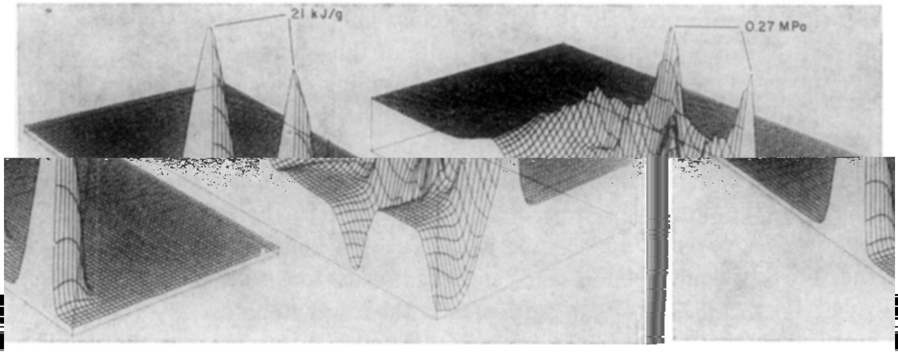

FIG. 7. Surfaces of specific internal energy (left) and pressure (right) in the r–z computing mesh at 100 msec. The peak values are labeled in each plot.

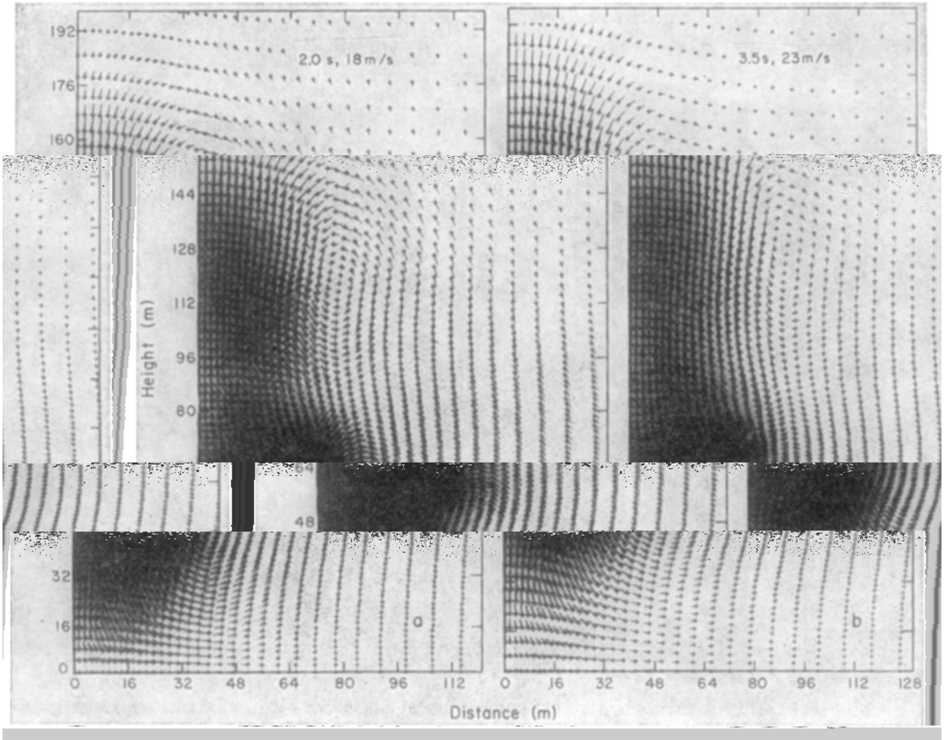

FIG. 8. Velocity vector plots at 2.0 and 3.5 sec.

shock with pressure peaks in the Mach stems. The blast wave is smoothed due to numerical diffusion in the larger mesh cells in the outer parts of the computing mesh (Fig. 6a). One notes in particular the softening of the shock above the upper bubble. Figure 7 also shows the pressure undershoot that occurs where the shocks collide and at the ground.

During the interval 0.1–1.0 sec the counterclockwise vortex in the lower bubble (Fig. 6d) becomes an inflection in the axial flow field. Figure 8 shows the flow at 2.0 and 3.5 sec, well after the blast wave's departure. The flow at 2 sec contains an "afterwind" moving inward toward the axis above the ground. This wind enters the clockwise vortex in the lower bubble.

Axial flow consists of updrafts into the top bubble. There is an inflection in the flow field 16 m below the symmetry plane (64 m height) and 16 m from the axis. The largest wind speed is 18 m/sec at 2 sec, and occurs in the updraft. Stagnation points are seen at 72 m height on the axis and at 80 m height, 45 m from the axis, as well as at the two centers of clockwise vorticity.

The counterclockwise vorticity decreases as the axial flow strengthens. Comparison of the 3.5 sec velocity vector plot with the 2.0 sec plot shows that the vortices in the upper and lower bubbles decouple. Figure 9 displays the contours of specific internal energy, density, and vorticity at 3.5 sec. These show that the

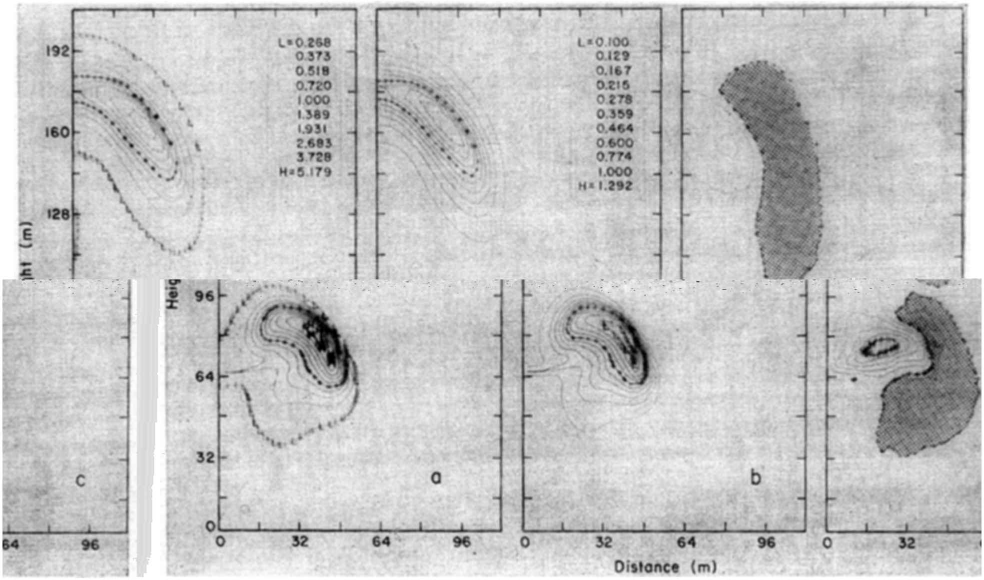

FIG. 9. (a) Logarithmic contours of specific internal energy in *J/kg* at 3.5 sec. (b) Logarithmic contours of density in mg/cm³. (c) Contours of scalar vorticity. Stippling indicates regions of negative (clockwise) vorticity.

problem indeed evolves into two buoyant vortex rings, the lower one being tighter (more developed) than the upper one.

Buoyancy causes the lower bubble to rise, and the flow field carries its material into the upper bubble's vortex ring. At about 5 sec the lower bubble's vortex disintegrates and its material enters into the top vortex. Figure 10 shows plots of Lagrangian marker particles at 1 sec intervals between 5 and 10 sec. The particles

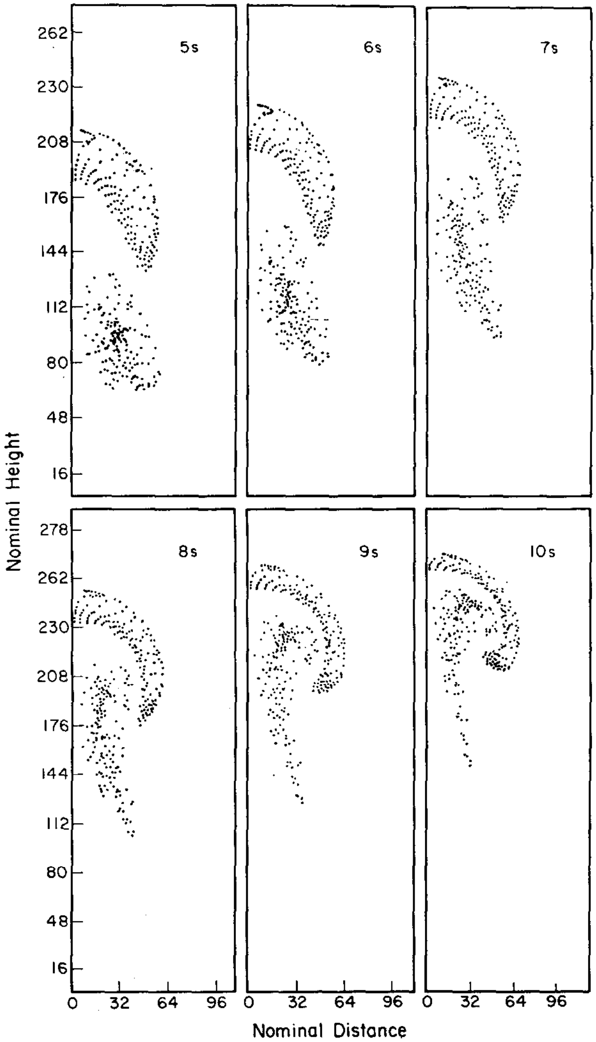

FIG. 10. Lagrangian marker particles at 1-sec intervals from 5 to 10 sec.

were initially distributed uniformly to mark the bubble material inside each 30-m-diameter sphere. The plot at 5 sec shows the distortion in the upper bubble due to shock reflection and the buoyancy forces. The particles in the lower bubble are caught in the suction (updraft) of the top bubble, and by 10 sec they are mostly entrained in the upper vortex. The particles are seen to mix toward the side, rather than to penetrate through the top of the ring as might be expected.

IV. S_n CALCULATIONS

The grey and nongrey S_n methods described previously were also used to solve the radiative phases of the two-bubble test problem. Figure 11 shows the cooling curve obtained with the implicit, S_4 (12 streams), grey method and the curve shown previously in Fig. 7. The nongrey S_4 curve lies slightly below the Monte Carlo result.

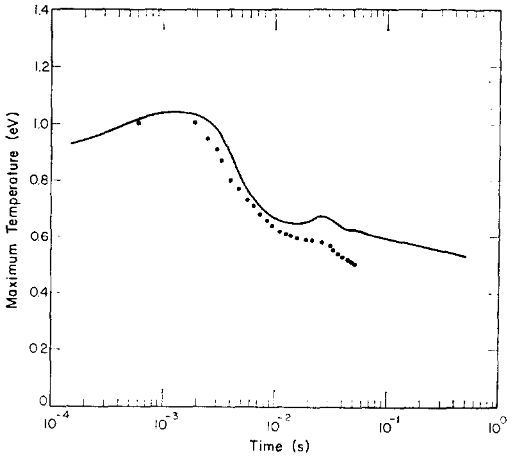

FIG. 11. Cooling curves computed with nongrey, Monte Carlo (solid line) and grey, S_n (dots)

Figure 12 shows vector plots of the net radiative flux in each computing cell at 11.4 and 14.7 msec. These plots show the net fluxes as vectors whose components are the appropriate angular moments of the specific intensity [5]. At 11.4 msec the bubbles are optically thick and the fluxes maximize in the temperature gradient where radiative losses occur. The bubbles become optically thinner as the air cools, and the plot at 14.7 msec shows that all the cells contain outward fluxes. Thus, when the bubbles are optically thick, the cooling rate is governed primarily by the temperature gradient in the outer layers, and when the bubbles become optically thin, at later times, by the opacity in the bubble volume.

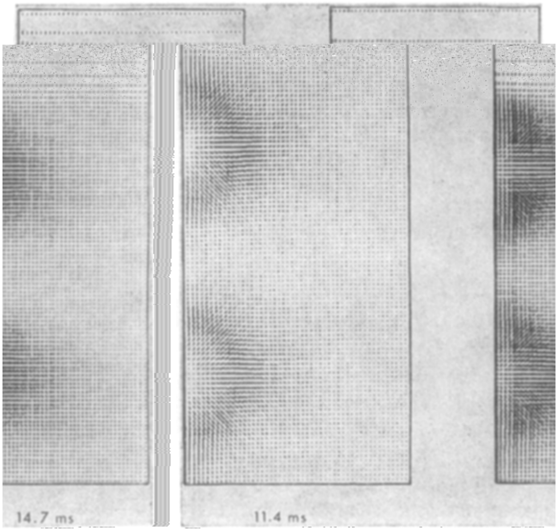

FIG. 12. Net radiative fluxes computed with the grey, S_n method.

V. DISCUSSION

Near-Lagrangian hydrodynamics (YAQUI) offers advantages over the Eulerian hydrodynamics (SIERRA) that we used previously, but it complicates the radiative transfer calculations. The Monte Carlo method can usefully interface with distorted cells if one is careful to optimize the geometry routines so that computing time is minimized. The S_n method is successful in solving the implicit, grey equation of transfer; but it demands rectangular cell geometry. The S_n and Monte Carlo methods are somewhat complementary in that we find regimes of application for each. We anticipate that a computational algorithm which couples the Monte Carlo and S_n methods in different parts of the same mesh would be of limited use because of the difficulties in the energy (flux) conservation scheme.

There remains the possible application of other iterative methods for solving the transfer equation which might give rapid, stable solution in optically thick, distorted cells. The Variable Eddington (VERA) or moment method does not appear useful because its rigorous application requires angular radiances to evaluate the moment equations. The radiances must be calculated with difference methods like S_n, or the diffusion approximation used to obtain the moments directly. Thus, the method reduces to one like S_n or it dispenses with radiative transfer altogether.

ACKNOWLEDGMENTS

We thank William R. Reed for providing us with the S_n code. Eric M. Jones assisted with implementing YAQUI hydrodynamics. Norma Butler and Barbara Anderson typed numerous drafts and suffered in silence.

REFERENCES

1. M. T. SANDFORD AND R. C. ANDERSON, *J. Computational Phys.* **13** (1973), 130.
2. C. W. HIRT, A. A. AMSDEN, AND J. L. COOK, *J. Computational Phys.* **14** (1974), 227.
3. F. HARLOW AND A. A. AMSDEN, *J. Computational Phys.* **8** (1971), 197.
4. K. D. LATHROP AND F. W. BRINKLEY, TWOTRAN-II: An Interfaced, Exportable Version of the TWOTRAN Code for Two-Dimensional Transport, Los Alamos Scientific Laboratory Report LA-4848-MS, 1973.
5. W. REED, private communication, 1972.
6. J. A. FLECK AND J. D. CUMMINGS, *J. Computational Phys.* **8** (1971), 313.
7. I. M. SWIFT AND D. C. SACHS, Operation Upshot–Knothole Project 1.1b: Air Pressure and [redacted]